# Magma fragmentation in highly explosive basaltic eruptions induced by rapid crystallisation

Fabio Arzilli[1], Giuseppe La Spina[1], Mike R. Burton[1], Margherita Polacci[1], Nolwenn Le Gall[2], Margaret E. Hartley[1], Danilo Di Genova[3], Biao Cai[4], Nghia T. Vo[5], Emily C. Bamber[1], Sara Nonni[5], Robert Atwood[5], Edward W. Llewellin[6], Richard A. Brooker[7], Heidy M. Mader[7] and Peter D. Lee[2]

[1]School of Earth and Environmental Sciences, University of Manchester, Manchester M139PL, UK

[2]Department of Mechanical Engineering, University College London, London, UK

[3]Institute of Non-Metallic Materials, Clausthal University of Technology, Zehntner Str. 2a, 38678 Clausthal-Zellerfeld, Germany

[4] School of Metallurgy and Materials, University of Birmingham, Birmingham B15 2TT, UK

[5]Diamond Light Source, Harwell Science and Innovation Campus, Didcot OX11 0DE, UK

[6]Department of Earth Sciences, Durham University, Durham DH1 3LE, UK

[7]School of Earth Sciences, University of Bristol, Bristol BS8 1RJ, UK

[*]Corresponding author: Dr. Fabio Arzilli

Corresponding author present affiliation: School of Earth and Environmental Sciences, The University of Manchester, Oxford Road, Manchester, M13 9PL, UK

E-mail address: fabio.arzilli@manchester.ac.uk

Phone: +393298429732; +447904104670

**Basaltic eruptions are the most common form of volcanism on Earth and planetary bodies. The low viscosity of basaltic magmas inhibits fragmentation, favouring effusive and lava-fountaining activity, yet highly explosive, hazardous basaltic eruptions occur. The processes that promote fragmentation of basaltic magma remain unclear and are subject to debate. Here we use a numerical conduit model to show that rapid magma ascent during explosive eruptions produces large undercooling. In situ experiments reveal that undercooling drives exceptionally rapid (~minutes) crystallisation, inducing a step-change in viscosity that triggers magma fragmentation. Experimentally produced textures are consistent with basaltic Plinian eruption products. We apply a numerical model to investigate basaltic magma fragmentation over a wide parameter space and find that all basaltic volcanoes have the potential to produce highly explosive eruptions. The critical requirements are initial magma temperatures lower than 1100 °C to reach a syn-eruptive crystal content of over 30 vol.%, and thus a magma viscosity around $10^5$ Pa s, which our results suggest is the minimum viscosity required for the fragmentation of fast ascending basaltic magmas. These temperature, crystal content and viscosity requirements reveal how typically effusive basaltic volcanoes can produce unexpected highly explosive and hazardous eruptions.**

Explosive eruptions are the most violent expression of volcanic activity[1,2]. Highly explosive Plinian eruptions can eject > 0.1 $km^3$ of pyroclastic material producing volcanic plumes that can reach up to 40 km in height, impacting both regional and global climate, and producing a significant threat to proximal populations[3,4]. Basaltic volcanoes are usually characterised by effusive and mildly explosive lava fountaining activity[5], however, basaltic Plinian eruptions can also occur[6-11]. The main process producing highly explosive activity is brittle magma fragmentation, which is the transition from a continuous liquid phase in which crystals and bubbles are suspended to a continuous gas phase carrying fragments of magma[1,2]. For silicic magmas, brittle fragmentation is attributed to high strain rates associated with acceleration of the bubbly mixture[1,12-14] or to bubble overpressure associated with restricted bubble expansion[14,15-18]. However, the low viscosity of basaltic magma makes the high strain rates or bubble overpressure necessary to trigger fragmentation difficult to achieve[1,19].

Crystallisation during magma ascent may significantly increase magma viscosity, leading to fragmentation[20]. However, crystallisation in basaltic magmas has previously been thought to occur on timescales significantly longer than the time required for magma to ascend from a crustal storage chamber to the vent[21], particularly in the case of highly explosive eruptions.

In volcanic conduits, the crystallisation kinetics of an ascending magma are driven by degassing and cooling[22-23]. Plagioclase and pyroxene crystallisation are sensitive indicators of magma dynamics in volcanic conduits[21,24-27] and their kinetically controlled abundance can rapidly change magma rheology[28-29]. Our understanding of crystallisation kinetics in magmas is underpinned by crystallisation quench experiments in which there is no *in situ* visualisation (henceforth termed '*ex situ*' experiments). Here we perform novel experiments of rapid crystallisation in basaltic magmas with *in situ* visualisation (henceforth termed '*in situ*' experiments) in order to quantify in real time when crystals start to form and how quickly magma crystallinity evolves.

A frequently used model to describe crystallisation as function of time is given by an exponential law[21,23], where the rate of crystallisation is controlled by the characteristic time $\tau^{(c)}$. The

characteristic time is a measure of how fast a process will approach the equilibrium[21,30]. The smaller $\tau^{(c)}$, the faster crystals reach their equilibrium abundance (see Methods section). La Spina et al. (ref. 21) demonstrate that ~4.6 times $\tau^{(c)}$ is the time required to reach the equilibrium crystal fraction in basalts. During mild lava-fountaining basaltic activity[21], $\tau^{(c)}$ is of the order of 1000 s, resulting in a crystallisation time of ~2 hours. The crystallisation rate increases with increasing magma ascent rate, as cooling and decompression rates increase[30-34]. Thus, for fast-ascending magmas, $\tau^{(c)}$ is smaller and the equilibrium crystal fraction will be reached faster. However, the characteristic times of crystal growth during fast magma ascent have not been quantified.

In order to quantify the characteristic times of plagioclase and pyroxene crystallisation during rapid ascent of basaltic magma, we conducted the first *in situ* 4D (3D plus time) crystallisation kinetics experiments under fast cooling rates, using fast synchrotron X-ray microtomography. Our experiments provide the first estimation of the characteristic time for plagioclase and pyroxene crystallisation in trachybasaltic magmas during a rapid and continuous increase of undercooling, where $\Delta T$ is defined as the difference between the highest temperature at which plagioclase and pyroxene is expected to crystallise and the temperature of the magma[24-27].

**Crystallisation experiments at high undercooling**

Crystallisation experiments were performed *in situ* at beamline I12-JEEP, Diamond Light Source, Harwell, UK, using a trachybasaltic glass (Supplementary Table 1) from the 2001 Etna eruption as the starting material (see Methods). We combined a bespoke high-temperature environmental cell[35] with fast synchrotron X-ray microtomography to image the evolution of crystallisation in real time[36] in two experiments. In the first part of the experiment, crystallisation was induced by decreasing temperature from 1250 °C to either 1170 °C or 1150 °C at 0.4 °C $s^{-1}$ at ambient pressure with a dwell time at the final temperature of 4 h[36] (Supplementary Fig. 1). During these 4 h, blocky and prismatic clinopyroxene and oxide crystals were grown[36] (Fig. 1 and Supplementary Figs. 2 and 3), and the residual melt evolved to a basaltic trachyandesite

composition (Supplementary Table 1). After 4 h at sub-liquidus conditions (either 1170 °C or 1150 °C), the system was cooled at a rate of 0.4 °C $s^{-1}$. This induced a sudden and continuous undercooling ($\Delta T$) resulting in a rapid crystallisation event of plagioclase and clinopyroxene (Fig. 1; Supplementary Figs. 2 and 3). Skeletal plagioclase crystals grew during this final stage of rapid cooling, specifically between 1112 and 1073 °C after a dwell time of 4 hours at 1150 °C (Fig. 1) and between 1131 and 1053 °C after a dwell time of 4 hours at 1170 °C (Supplementary Fig. 3a,b,c). Plagioclase crystals grew to equilibrium abundance (~10 vol.%) in ~90 seconds (Fig.1a,b), i.e. between two 3D scans, reaching sizes between ~30 and ~500 µm. Following the initial burst of rapid plagioclase growth, dendritic clinopyroxene crystals (augitic composition) nucleated heterogeneously on plagioclase (labradoritic composition) and grew to their final abundance (~65 vol. %) in the following 180 seconds (Fig. 1b,c; Supplementary Figs. 2b,c, 3d,e, and 4), resulting in almost complete crystallisation of the sample. Dendritic clinopyroxene crystals developed by diffusion-controlled branching growth in multiple directions, reaching a maximum crystal length between 30 and 40 µm (Supplementary Fig. 3d,e).

The large $\Delta T$ reached in a relatively short time during our *in situ* 4D crystallisation experiments generated distinctive skeletal plagioclase crystals with swallow-tail morphology and dendritic pyroxene (Fig. 2a-c), similar to the skeletal plagioclase and dendritic pyroxene crystals observed in the products of explosive basaltic Plinian eruptions[7-11,37,38], such as Etna 122 B.C.[7,8,37,38] (Fig. 2d). These distinctive textures are also reported in products of the Fontana Lapilli (Nicaragua)[11,37,38] and 1886 Tarawera (New Zealand) eruptions[7,9,10]. The signature skeletal plagioclase and dendritic pyroxene is also observed in sub-Plinian eruption (Yufune 2) products of Mt. Fuji (Japan)[39].

Skeletal plagioclase crystallisation occurred at $\Delta T$ between 60 and 140 °C with a growth rate between $3x10^{-5}$ and $1x10^{-4}$ cm $s^{-1}$ (1 to 4 mm $h^{-1}$) (Supplementary Table 2), whilst dendritic pyroxene crystallised at $\Delta T$ between 60 and 175 °C with a growth rate of $2x10^{-5}$ cm $s^{-1}$ (0.7 mm $h^{-1}$) (Supplementary Table 2). This indicates that a rapid increase of $\Delta T$ (>60 °C) induces fast crystallisation. As the equilibrium pyroxene crystal content is achieved within ~180 s, we can infer

that the pyroxene characteristic time under large $\Delta T$ is < 40 s. For plagioclase, the equilibrium crystal content is achieved within 90 s and the characteristic time is < 20 s. These are about two orders of magnitude less than the characteristic time for effusive and mild lava fountaining activity at Etna (Italy), Stromboli (Italy) and Kilauea (Hawaii), which involved much smaller ΔT (30-60 °C)[21] and magma ascent rates of ~3 m $s^{-1}$.

To corroborate results from *in situ* 4D experiments, *ex situ* experiments were also performed using a TZM cold seal pressure vessel apparatus, in order to investigate whether fast crystallisation also occurs in hydrous trachybasaltic melt during rapid and continuous cooling and decompression (see Methods), simulating fast magma ascent in the conduit. The experimental approach consisted of holding the sample for 30 minutes at 75 MPa and 1070 °C before decompression and cooling. After 30 minutes, pressure and temperature were decreased continuously for 300 s at 0.2 MPa $s^{-1}$ and 0.2 °$Cs^{-1}$ respectively, reaching 15 MPa and 1010 °C (Supplementary Table 3; Supplementary Fig. 5). The rapid decompression and cooling achieved a large ΔT of >100 °C (Supplementary Fig. 5) in 300 s, favouring predominantly clinopyroxene crystallisation with minor plagioclase and oxide (Supplementary Fig. 6). This indicates that $\tau^{(c)}$ is < 60 s, in agreement with the order of magnitude estimated from *in situ* experiments.

Large undercooling can produce significant syn-eruptive microlite crystallisation during rapid magma ascent[24-27]. This increase in crystallinity dramatically increases the viscosity of the magma[19]. This process has been proposed to explain explosive basaltic Plinian eruptions, supported by evidence of high microlite contents in erupted products[7-11,37,38]. However, a mechanism for this exceptionally fast crystallisation during rapid magma ascent in basaltic Plinian eruptions, favouring fragmentation, has not been demonstrated so far.

**Etna basaltic Plinian eruption numerical simulation**

Magma fragmentation in basaltic Plinian eruptions has been investigated with conduit models, where crystallisation has been assumed either to be constant[20] or at equilibrium[40]. Recent results

demonstrate that disequilibrium crystallisation plays a fundamental role in magma dynamics within the conduit[21], but syn-eruptive disequilibrium crystallisation has not yet been considered for basaltic explosive volcanism[20,40].

We used the conduit model described by La Spina et al. (ref. 21, 23) to investigate the effect of the new experimentally constrained characteristic times for crystallisation with large undercooling on the ductile-brittle transition of basaltic magma during highly explosive eruptions. Since we are focusing our attention on explosive eruptions with high mass eruption rates (>$10^6$ kg/s), it is reasonable to assume that outgassing is negligible for this kind of activity. Indeed, outgassing will be inhibited by fast magma ascent as fragmentation will be achieved faster than outgassing[41]. As a test case, we consider the 122 B.C. Etna basaltic Plinian eruption[6-8]. To model fragmentation we adopt the strain rate criterion introduced by Papale (ref. 1):

$$\dot{\gamma} = k\frac{G_\infty}{\mu} \tag{1}$$

where $\dot{\gamma}$ is the elongational strain rate, $k$=0.01 is a constant, $\mu$ is the magmatic viscosity and $G_\infty$ is the elastic modulus at infinite frequency. Constitutive equations for the numerical model are reported in the Methods section. In Figure 3 we report the calculated plagioclase undercooling, crystal content and viscosity as function of depth for $\tau^{(c)}$ = 10 and 1000 s. For $\tau^{(c)}$ = 10 s, large undercooling is produced by adiabatic expansion of exsolved volatiles and mitigated by the latent heat of crystallisation (Fig. 3a). In this case, numerical results show a rapid increase in crystallinity and in viscosity at depths below 2 km (Fig. 3c), leading to fragmentation and explosive Plinian eruption. Importantly, numerical results indicate that strain-induced fragmentation is favoured by a combination of rapid viscosity increase (about one order of magnitude in 5 seconds approaching the fragmentation depth) and fast decompression and ascent rates (~0.2 MPa $s^{-1}$ and ~15 m $s^{-1}$) that generate high strain rates. For $\tau^{(c)}$ = 1000 s, the crystallisation rate is slow and viscosity stays within the fragmentation threshold throughout the conduit.

**Basaltic magma fragmentation sensitivity analyses**

Having established that fast crystallisation plays an important role in basaltic Plinian eruptions, we performed a sensitivity analysis with the numerical model described by La Spina et al. (ref. 21, 23) to investigate the parameter space whereby basaltic fragmentation driven by rapid crystallisation may occur. We use the Etna 122 B.C. eruption as a test case. We focus on the behaviour of $\Delta T$ as a function of characteristic time of crystallisation, pressure, temperature and total magmatic $H_2O$ content (dissolved plus exsolved) at the conduit inlet, conduit radius, and initial phenocryst content. A detailed description of the initial conditions of the sensitivity study can be found in the Methods section. We performed several sensitivity analyses assuming a characteristic time of $\tau^{(c)}$ = 10 s as observed in *in situ* experiments, and $\tau^{(c)}$ = 1000 s as observed for Etna 2001 in mildly explosive activity. We also examined $\tau^{(c)}$ = 1 and 100 s for completeness.

Numerical results show that undercooling is principally controlled by $\tau^{(c)}$ (Fig. 4a), because the release of latent heat during rapid crystallisation (i.e. small $\tau^{(c)}$) affects the temperature of the system and consequently the undercooling. Therefore, undercooling and characteristic time are coupled. However, our numerical results indicate that within the parameter space investigated, $\Delta T$ is always maintained between 60 and 190 °C (Fig. 4b), which is enough to enable rapid crystallisation in any case. The sensitivity analyses indicate that, besides the characteristic time, initial temperature and total water content play an important role in controlling undercooling (Fig. 4a). $\Delta T$ at the point of fragmentation increases as initial temperature decreases (Fig. 4b), meaning that cooler magma in the chamber is more likely to produce microlite crystallisation during ascent, as $\Delta T$ will already be large under pre-eruptive conditions. An increase in the initial total $H_2O$ also produces an increase of $\Delta T$ (Fig. 4c), caused by greater cooling of the system, a result of enhanced adiabatic gas expansion. Higher water contents favour rapid microlite crystallisation, attributed to the increase in cation diffusivity within the silicate melt[42].

Sensitivity analyses show that a lower initial temperature and a higher pre-eruptive crystal content results in a greater likelihood of explosive eruptions (Fig. 4d,e). This is consistent with

estimates of pre-eruptive temperatures obtained for the Etna and Fontana Plinian eruptions, which range between 1000 and 1060 °C[37]. However, the products of basaltic Plinian eruptions are characterised by a small phenocryst content (<10 vol.%)[7,8,10,11,37,38,40]. Therefore, in this context of low initial temperature and low phenocryst content, numerical results highlight that the characteristic time of crystallisation plays a fundamental role in increasing likelihood of an explosive eruption. A small $\tau^{(c)}$ is the primary cause for a significant increase of the syn-eruptive crystal fraction over short timescales during magma ascent, which consequently increases magma viscosity and thus the probability of magma fragmentation (Fig. 4f). Furthermore, our sensitivity analysis demonstrates that when the syn-eruptive crystal content exceeds 30 vol.%, all numerical solutions reach the fragmentation threshold (Fig. 4f). In a fast-ascending magma (from our sensitivity analyses we have an ascent rate that ranges between 5 and 50 m $s^{-1}$), the predicted increase in syn-eruptive crystal content produces a rapid and dramatic increase in viscosity (about one order of magnitude in less than 10 s close to the fragmentation depth), increasing the likelihood of magma fragmentation. Numerical results also show that as soon as viscosity exceeds $10^5$ Pa s, all the numerical solutions reach the fragmentation threshold, generating an explosive eruption (Fig 4g). For a fast-ascending magma where outgassing can be neglected and strain rates are high, the key parameter controlling the triggering of fragmentation is viscosity. Therefore, $10^5$ Pa s represents a minimum viscosity determining a drastic change in eruptive style for explosive activity characterised by high mass eruption rates. This minimum viscosity is one order of magnitude lower than previously reported for low-viscosity magmas[1,43].

The remarkable insights provided by novel *in situ* observations of crystallisation provide a new research frontier for studies of crystallisation kinetics. Our *in situ* experimental and natural observations combined with a numerical model allow us to conclude that pre-eruptive temperatures <1100 °C favour the formation of highly explosive basaltic eruptions, such as Plinian volcanism, driven by fast syn-eruptive crystal growth under high undercooling and high decompression rates.

This implies that all basaltic systems on Earth have the potential to produce powerful explosive eruptions.

## METHODS

**Starting material.** The starting material used for our crystallisation experiments is a trachybasalt from the lower vents of the 2001 Mt Etna eruption[36,44]. The anhydrous glassy starting material was synthesized by melting a crushed rock sample in a Pt crucible. Melting was performed in a Nabertherm® $MoSi_2$ box furnace at 1400 °C and at atmospheric pressure. The melt was left in the furnace for 4 hours to allow the melt to fully degas and to dissolve any crystals present. The melt was then quenched in air to glass. This procedure was repeated two times to homogenise the melt. Finally, anhydrous glassy cylinders 3 mm in diameter and 4 mm in length were drilled from the synthesized glass for *ex situ* and *in situ* 4D crystallisation experiments.

The chemical composition of the anhydrous glassy starting material was analysed with a Jeol JXA 8530 F microprobe at the Photon Science Institute, University of Manchester, UK, and is reported in Supplementary Table 1. Analyses were performed using a 15 kV accelerating voltage, 10 nA beam current and beam size of 10 μm. Standards used for calibration were albite for Na, periclase for Mg, corundum for Al, fayalite for Fe, tephroite for Mn, apatite for P, sanidine for K, wollastonite for Ca and Si and rutile for Ti. Na and K were measured first to minimize loss owing to volatilisation.

Hydrous trachybasaltic glass with ~3 wt.% $H_2O$ was obtained by melting the starting material (Supplementary Table 1) and homogenising with $H_2O$ in a Pt capsule at 100 MPa and 1200 °C. The hydrous starting glasses were produced using a TZM cold seal pressure vessel apparatus at the School of Earth Sciences, University of Bristol, UK. Before performing crystallisation experiments, the loaded 3 wt.% water content of the starting material was confirmed to be present in the glass by Fourier Transform Infrared (FTIR) spectroscopy using a Nicolet i10 spectrometer, a MCT detector and an extended range KBr beamsplitter. Using the density trend and Etna basalt extinction coefficient of Lesne et al. (ref. 45), the molecular $H_2O$ peak at 5200 $cm^{-1}$ gives 1.71 wt.% and the OH peak at 4500 $cm^{-1}$ gives 1.38 wt.% water, a total of 3.09 wt.% with the correct species proportions for the total water content.

252

253 ***Ex situ* decompression and cooling experiments.**

254 *Ex situ* experiments were performed in order to investigate the process of fast crystallisation in a
255 hydrous trachybasaltic melt during continuous decompression (0.2 MPa $s^{-1}$) and cooling (0.2 °$Cs^{-1}$),
256 simulating magma ascent in the conduit. Two experiments were performed using a TZM cold seal
257 pressure vessel apparatus at the School of Earth Sciences, University of Bristol, UK. The redox
258 condition of the apparatus maintained at NNO by adding ~1 vol.% of hydrogen to the pressuring
259 argon. Capsules ($Au_{80}$-$Pd_{20}$) were loaded with hydrous glass cylinders. The experimental approach
260 consisted of holding the sample for 30 minutes at 75 MPa and 1070 °C before being decompressed
261 and cooled. The first experiment was quenched after 30 minutes at 75 MPa and 1070 °C, in order to
262 characterise the crystallinity and texture at the point before fast decompression and cooling were
263 applied. In the second experiment, after 30 minutes pressure and temperature were released
264 continuously over 300 s at 0.2 MPa $s^{-1}$ and 0.2 °$Cs^{-1}$ respectively, reaching 15 MPa and 1010 °C
265 (Supplementary Table 3; Supplementary Fig. 5) before quenching at these conditions. The selected
266 decompression and cooling rates represent numerical predictions of the conduit model for magma
267 ascent during basaltic Plinian eruptions. The final pressure represents the most likely fragmentation
268 pressure.

269

270 ***In situ* synchrotron X-ray microtomography experiments.**

271 The experiments were performed at the beamline I12-JEEP[46], Diamond Light Source, Harwell,
272 UK. For these *in situ* crystallisation experiments we used the high-temperature resistance Alice
273 furnace[47], which allows us to control cooling at 0.05 °$Cs^{-1}$ to 0.4 °$Cs^{-1}$, and the sample stage
274 mounted on the beamline I12-JEEP[46] for high-speed rotation. Temperature was measured with an
275 R-type thermocouple positioned close to the sample in the middle of the furnace hot spot. The
276 furnace hot spot with homogeneous temperature measures a volume of ~5x5x5 mm, and our
277 samples were positioned within this area. The R-type thermocouple measures the sample

temperature with an uncertainty of ±5 °C. The sample holder was an alumina crucible (Supplementary Fig. 2), which is suitable for the temperature range investigated and has a low X-ray attenuation coefficient. The glassy cylinders were heated *in situ* in the Alice furnace and held at 1250 °C for 30 minutes (Supplementary Fig. 1). After the initial annealing period, crystallisation was induced by decreasing temperature from 1250 °C to 1170 °C or 1150 °C at ambient pressure, holding at the final temperature for 4 h[36] (Supplementary Fig. 1). After this step, the system was cooled at rate of 0.4 °C$s^{-1}$ in order to investigate the rapid crystallisation at high undercooling (up to ~180 °C) in real time (Supplementary Fig. 1).

The experiments were performed in phase-contrast mode, setting the sample-to-detector distance at 2300 mm in order to work in the edge-detection regime[48] (Supplementary Table 4). The projections were acquired using a monochromatic X-ray beam with energy of 53 keV. In each scan, 1800 tomographic projections were acquired by the detector with equiangular steps over a full rotation angle of 180° (Supplementary Table 4). The exposure time for the acquisition of each projection was 0.05 s (Supplementary Table 4), thus the temporal resolution of each scan was 90 seconds. The isotropic pixel size was 3.2 μm. The detector was a high-resolution imaging PCO edge camera with optical module 3, corresponding to a field of view of 8.0 mm × 7.0 mm. Scan acquisition started before the end of the annealing and covered the cooling period between 1250 °C and the dwell temperatures (1170 and 1150 °C), the entire duration of the dwell time, and the final rapid cooling at 0.4 °C $s^{-1}$.

**Image reconstruction and processing.** Tomographic projections were reconstructed into 32-bit slices using Diamond I12 in-house python codes, using the *gridrec* algorithm[49,50] (http://confluence.diamond.ac.uk/display/I12Tech/Reconstruction+scripts+for+time+series+tomography)[51,52]. The pre-processing pipeline includes centre of rotation calculation[50], zinger removal, blob removal[51], and regularisation-based ring removal[53].

303 The reconstructed slices were converted to 8-bit raw format and stacked using ImageJ software[54]
304 to obtain volumes in which the isotropic voxel has an edge size of 3.2 μm. Reconstructed volumes
305 of experiments ET1150 and ET1170 were then cropped using Avizo® software v.8.0 (FEI
306 Visualization Sciences Group) in order to select the volume of interest (VOI) (Supplementary Table
307 4). In experiment ET1150 plagioclase and pyroxene crystals nucleated and grew in a relatively large
308 pocket of melt (Figs. 1 and 2). Therefore, the VOI selected consists of a volume of melt where rapid
309 crystallisation of plagioclase and pyroxene occurred during the final cooling rate of 0.4 $°Cs^{-1}$.
310 Similarly, in experiment ET1170 plagioclase and pyroxene crystals formed in narrow layers of melt
311 (Supplementary Fig. 3) during rapid continuous cooling at 0.4 $°Cs^{-1}$.
312 Three-dimensional visualisation (volume rendering) of the reconstructed volumes was obtained
313 using the commercial software VGStudio 3.0 (Volume Graphics), which allowed us to make 3D
314 textural observations of the plagioclase and pyroxene crystal morphologies (Fig. 2). The
315 reconstructed volume of each scan allowed us to quantify when and at what range of temperatures
316 plagioclase and pyroxene crystals were able to grow.
317
318 **Image segmentation and analysis of plagioclase**. Segmentation is the process that allows
319 separation of objects from the background to obtain binary volumes containing only the feature of
320 interest. Segmentation of plagioclase crystals from the glassy matrix was performed using semi-
321 automatic volume segmentation[55,56] in Avizo software v. 8.0 (Supplementary Table 4). This
322 segmentation requires manual drawing of the outlines of crystals on the 2D slices. This is repeated
323 every 5–10 slices, depending on the size of the crystal and the complexity of their shape, along the
324 crystal length. The crystal shape is reconstructed automatically by the software through an
325 interpolation procedure. The advantage of this technique is that the operator can verify the real
326 morphology of the object of interest by visual inspection[55,56].
327 The reconstructed segmented 3D images were processed and analysed with the Pore3D software
328 library, custom-developed at Elettra[57]. The Pore3D software allowed us to quantify the number of

329 plagioclase crystals and the volume and maximum length of each crystal, operating directly in the
330 3D domain[57,58]. From the 3D shapes of plagioclase crystals and their real maximum axis lengths
331 ($L_{3D}$) we calculated the growth rate ($Y_{L3D}$) of plagioclase crystals (Supplementary Table 2), using
332 the experimental growth duration . The growth rate was estimated using the following equation[54]:

333 $$Y_{L3D} = (L_{3D}*0.5)/t_{growth}$$

334 where $t_{growth}$ is the time required for crystal growth.

335

336 **Image analysis of pyroxene growth kinetics.** Back-scattered electron (BSE) images were
337 collected using a JEOL JSM-6390LA FE-SEM at the School of Earth and Environmental Sciences,
338 University of Manchester, UK, in order to analyse pyroxene morphologies and kinetics. We used an
339 acceleration voltage of 15 kV and beam current of 10 nA. The sizes of dendritic pyroxene crystals
340 were measured in the 2D domain using BSE images and ImageJ software[54], as the pyroxene
341 morphologies formed during continuous cooling in our *in situ* 4D crystallisation experiments are
342 difficult to resolve and analyse in the 3D domain. The pyroxene growth rate is calculated by
343 dividing the entire length of the dendritic crystal over the duration of pyroxene growth
344 (Supplementary Table 2).

345

346 **Electron microprobe analysis.** Samples obtained during *ex situ* and *in situ* crystallisation
347 experiments were analysed with a JEOL JXA-8530F field emission electron microprobe at the
348 Photon Science Institute, University of Manchester, UK. The operating conditions were as follows:
349 15 kV accelerating voltage, 10 nA beam current, and beam diameter of 10 or 5 μm (the latter for
350 dendritic and acicular microlites). Na and K were measured first to minimise loss by volatilisation.
351 Calibration standards were albite for Na, periclase for Mg, corundum for Al, fayalite for Fe,
352 tephroite for Mn, apatite for P, sanidine for K, wollastonite for Ca and Si and rutile for Ti.

353

**Constitutive equations for the conduit model.** In this work we use the 1D steady-state model for magma ascent described by ref. (21, 23, 59). The governing equations used in this work are reported in ref. (59). The application to a specific volcano is achieved by providing constitutive equations to describe the specific rheological, solubility, crystallisation, outgassing, and fragmentation behaviour of the system.

Following ref. (60), the viscosity of the liquid phase is modelled as:

$$\mu_l = \mu_{melt} \cdot \theta(x_c^l),$$

where $\mu_{melt}$ is the viscosity of the bubble-free, crystal-free liquid phase and $\theta$ is a factor which increases viscosity attributed to the presence of crystals[61].

We use an empirical relationship to estimate $\mu_{melt}$ as a function of dissolved water concentration and temperature, as in ref. (62) (based on the Vogel-Fulcher-Tammann equation):

$$\log(\mu_{melt}) = \mathrm{A} + \frac{\mathrm{B}(\mathrm{y}, x_{d_{H_2O}}^{md})}{T - \mathrm{C}(\mathrm{y}, x_{d_{H_2O}}^{md})},$$

where the viscosity $\mu_{melt}$ is in Pa s and $T$ is the temperature in Kelvin. Parameter A is the logarithmic value of the viscosity at infinite temperature and is assumed to be constant for all melts. Parameters B and C are functions of the melt composition $y$ and of the dissolved water content $x_{d_{H_2O}}^{md}$. In this work, the melt composition is taken as the mean crystal-hosted melt inclusion composition from Etna 122 B.C. erupted products[63]. As crystallisation proceeds, viscosity increases according to the empirical model described in ref. (64):

$$\theta = \frac{1 + \varphi^{\delta}}{[1 - F(\varphi, \xi, \gamma)]^{B\phi^*}},$$

where

$$F = (1 - \xi) erf\left[\frac{\sqrt{\pi}}{2(1 - \xi)} \varphi(1 + \varphi^{\gamma})\right], \qquad \varphi = \frac{\left(\sum_{j=1}^{n_c} x_{c_j}^l\right)}{\phi^*}.$$

The fitting parameters $B, \delta, \xi, \gamma$ and $\phi^*$ chosen for this work are the same as those used in ref. (65).

Our numerical conduit model takes into account two different gas components: water and carbon dioxide. The equilibrium profile of the dissolved gas content $x_{d_i}^{md,eq}$ of component $i$ follows the Henry's Law, i.e.

$$x_{d_i}^{md,eq} = \sigma_i \left(\frac{P_{g,i}}{\bar{P}}\right)^{\varepsilon_i},$$

where $P_{g,i} = \alpha_{g_i} P_g / \alpha_g$ is the partial pressure of the $i$-th gas component expressed in $Pa$, $\bar{P} = 1$ Pa is used to make the expression in the brackets adimensional, $\sigma_i$ is the solubility coefficient and $\varepsilon_i$ is the solubility exponent. We assume that the solubility parameters $\sigma_i$ and $\varepsilon_i$ are constant during ascent. We adopted the following parameters $\sigma_{H_2O} = 1.8911 \times 10^{-6}$; $\varepsilon_{H_2O} = 0.5257$; $\sigma_{CO_2} = 2.2154 \times 10^{-12}$; $\varepsilon_{CO_2} = 1.075$. We also assume equilibrium exsolution, which means that the dissolved volatile contents always follow the equilibrium profile.

The crystallisation model adopted here has been proposed in ref. (23). We consider the three major crystal components erupted by Etna volcano: plagioclase, pyroxene and olivine. We assume that crystals stay coupled with the melt (i.e. no fractional crystallisation). For a better modelling of crystal nucleation and growth, we also assume that the equilibrium crystal contents are functions of temperature, pressure and dissolved water content. With these assumptions, the equilibrium mass fraction $x_{c_j}^{l,eq}$ of crystal phase $j$ is computed using the polynomial function

$$x_{c_j}^{l,eq}(P^*, T^*, x_d^*) = \zeta_{j,1}(P^*)^2 + \zeta_{j,2}(T^*)^2 + \zeta_{j,3}(x_d^*)^2 + \zeta_{j,4}(P^*)(T^*) +$$

$$+\zeta_{j,5}(T^*)(x_d^*) + \zeta_{j,6}(x_d^*)(P^*) + \zeta_{j,7}(P^*) + \zeta_{j,8}(T^*) + \zeta_{j,9}(x_d^*) + \zeta_{j,10},$$

where $P^*$ is the liquid pressure expressed in bars, $T^*$ is the temperature expressed in Celsius degrees and $x_d^*$ is the dissolved water concentration in weight percent. From $x_{c_j}^{l,eq}$, the equilibrium crystal volume fraction $\beta_j^{eq}$ can be computed using the relation

$$\beta_j^{eq} = \frac{\rho_l x_{c_j}^{l,eq}}{\rho_{c_j}}.$$

The parameters $\zeta_{j,i}$ are calculated fitting the polynomial function over a large range of data

obtained at different pressures, temperatures and water contents with alphaMELTS[66], a command line version of MELTS[67]. The starting melt composition is taken as the mean melt inclusion composition for Etna 122 B.C.[63].

Disequilibrium crystallisation is considered in our model and characteristic time controls the time needed to reach equilibrium crystal content. The differential equation that describes the crystal volume fraction within the conduit is the following[21]:

$$\frac{\partial \alpha_l \rho_c \beta u_l}{\partial z} = -\frac{1}{\tau^{(c)}} \alpha_l \rho_c (\beta - \beta^{eq}).$$

Here, $\alpha_l$ is the volume fraction of the liquid phase, $\rho_c$ is the density of the crystals, $u_l$ is the velocity of the liquid phase, $z$ is the vertical axis, $\beta$ is the actual total crystal volume fraction, and $\beta^{eq}$ is the equilibrium total crystal volume fraction. If we multiply all the terms by the characteristic time $\tau^{(c)}$, we notice that the smaller the $\tau^{(c)}$, the smaller $(\beta - \beta^{eq})$ has to be. In other words, the smaller the characteristic time, the faster the equilibrium crystal volume fraction will be reached.

Formally, the characteristic time reflects the time required to reduce the difference between the actual and the equilibrium value to $e^{-1}$ (~37%) of the initial difference[21]. This means that if $\beta_0$ is the initial value of a physical parameter β (which in our case is the crystal volume fraction) and $\beta_{eq}$ is the equilibrium value in response to a perturbation of the system, at the characteristic time τ we have

$$\beta(\tau) = \beta^{eq} + e^{-1}(\beta_0 - \beta^{eq}).$$

The experimental phase diagram for Etna basalt from 122 B.C. eruption[37] provides the plagioclase and pyroxene liquidus at different pressures and temperatures, whilst the conduit model is able to track temperature evolution within the conduit. Combining both of these data, we can estimate ΔT with respect to the plagioclase and pyroxene liquidus during magma ascent.

As we are interested in highly explosive activity, we assume no relative velocity between gas and melt. Magma fragmentation is modelled using the strain rate criterion introduced by ref. (1).

**Initial condition for the sensitivity analysis.**

The range of input parameters adopted for the sensitivity analysis are the following: 140–160 MPa for the inlet pressure at 6000 m depth, 1050–1100 °C for the magma inlet temperature, 5–30 m for the radius of the conduit, 2.0–4.0 wt.% for the total (dissolved plus exsolved) water content, 0.1–2.0 wt.% for the total (dissolved plus exsolved) $CO_2$ content, 0–20 vol.% for the initial crystal volume fraction (i.e. phenocryst content), and 1–1000 s for the characteristic time of crystallisation. As we do not know the probability distribution of the input parameters, we have assumed a uniform distribution within the aforementioned ranges. The input parameters are assumed to vary independently of one another. The sensitivity analysis was performed using the DAKOTA toolkit (Design Analysis Kit for Optimization and Terascale Applications)[68], an open-source software developed at Sandia National Laboratories that provides a flexible and extensible interface between analysis codes and iterative systems analysis methods such as uncertainty quantification, sensitivity analysis, optimization, and parameter estimation.

**Data availability**

The authors declare that the data supporting the findings of this study are available within the article and its supplementary information file. The data that support the findings of this study are available from the corresponding author upon request.

**Code availability**

The authors declare that the algorithms of the custom code used in this study are available within the article and its supplementary information file. The code that supports the findings of this study is available upon request.

**References in the main paper**

1. Papale, P. Strain-induced magma fragmentation in explosive eruptions. *Nature* **397**, 425 (1999).

2. Dingwell, D. B. Volcanic Dilemma--Flow or Blow?. *Science* **273**, 1054-1055 (1996).

3. Carey, S. & Sigurdsson, H. The intensity of plinian eruptions. *Bull. Volcanol.* **51**, 28-40 (1989).

4. Wilson, L. Explosive volcanic eruptions—III. Plinian eruption columns. *Geophys. J. Inter.* **45**, 543-556 (1976).

5. Polacci, M., Corsaro, R. A. & Andronico, D. Coupled textural and compositional characterization of basaltic scoria: Insights into the transition from Strombolian to fire fountain activity at Mount Etna, Italy. *Geology* **34**, 201-204 (2006).

6. Coltelli, M., Del Carlo, P. & Vezzoli, L. Discovery of a Plinian basaltic eruption of Roman age at Etna volcano, Italy. *Geology* **26**, 1095-1098 (1998).

7. Houghton, B. F., Wilson, C. J. N., Del Carlo, P., Coltelli, M., Sable, J. E. & Carey, R. The influence of conduit processes on changes in style of basaltic Plinian eruptions: Tarawera 1886 and Etna 122 BC. *J. Volcanol. Geotherm. Res.* **137**, 1-14 (2004).

8. Sable, J. E., Houghton, B. F., Del Carlo, P. & Coltelli, M. Changing conditions of magma ascent and fragmentation during the Etna 122 BC basaltic Plinian eruption: Evidence from clast microtextures. *J. Volcanol. Geotherm. Res.* **158**, 333-354 (2006).

9. Houghton, B. F. & Gonnermann, H. M. Basaltic explosive volcanism: constraints from deposits and models. *Che. Erde-Geochem.* **68**, 117-140 (2008).

10. Sable, J. E. Houghton, B. F., Wilson, C. J. N. & Carey, R. J. Eruption mechanisms during the climax of the Tarawera 1886 basaltic Plinian eruption inferred from microtextural characteristics of the deposits. *Studies in Volcanology: The Legacy of George Walker. Spec. Publ. IAVCEI* **2**, 129-154 (2009).

11. Costantini, L., Houghton, B. F. & Bonadonna, C. Constraints on eruption dynamics of basaltic explosive activity derived from chemical and microtextural study: the example of the Fontana Lapilli Plinian eruption, Nicaragua. *J. Volcanol. Geotherm. Res.* **189**, 207-224 (2010).

12. Melnik, O. & Sparks, R. S. J. Nonlinear dynamics of lava dome extrusion. *Nature* **402**, 37 (1999).

13. Gonnermann, H. M. & Manga, M. Explosive volcanism may not be an inevitable consequence of magma fragmentation. *Nature* **426**, 432 (2003).

14. Gonnermann, H. M. Magma fragmentation. *Ann. Rev. Earth Planet. Sci.* **43**, 431-458 (2015).

15. Alidibirov, M. & Dingwell, D. B. Magma fragmentation by rapid decompression. *Nature* **380**, 146 (1996).

16. Zhang, Y. A criterion for the fragmentation of bubbly magma based on brittle failure theory. *Nature* **402**, 648 (1999).

17. Spieler, O., Kennedy, B., Kueppers, U., Dingwell, D. B., Scheu, B. & Taddeucci, J. The fragmentation threshold of pyroclastic rocks. *Earth Planet. Sci. Lett.* **226**, 139-148 (2004).

18. Kueppers, U., Scheu, B., Spieler, O. & Dingwell, D. B. Fragmentation efficiency of explosive volcanic eruptions: A study of experimentally generated pyroclasts. *J. Volcanol. Geotherm. Res.* **153**, 125-135 (2006).

19. Giordano, D. & Dingwell, D. Viscosity of hydrous Etna basalt: implications for Plinian-style basaltic eruptions. *Bull. Volcanol.* **65**, 8-14 (2003).

20. Moitra, P., Gonnermann, H. M., Houghton, B. F. & Tiwary, C. S. Fragmentation and Plinian eruption of crystallizing basaltic magma. *Earth Planet. Sci. Lett.* **500**, 97-104 (2018).

21. La Spina, G., Burton, M., Vitturi, M. D. M. & Arzilli, F. Role of syn-eruptive plagioclase disequilibrium crystallisation in basaltic magma ascent dynamics. *Nature Commun.* **7**, 13402 (2016).

22. Cashman, K. & Blundy, J. Degassing and crystallisation of ascending andesite and dacite. *Phil. Trans. R. Soc. A* **358**, 1487-1513 (2000).

23. La Spina, G., Burton, M. & de' Michieli Vitturi, M. Temperature evolution during magma ascent in basaltic effusive eruptions: a numerical application to Stromboli volcano. *Earth Planet. Sci. Lett.* **426**, 89–100 (2015).

24. Hammer, J. E. & Rutherford, M. J. An experimental study of the kinetics of decompression induced crystallization in silicic melt. *J. Geophys. Res.: Solid Earth* **107**, ECV-8 (2002).

25. Couch, S., Harford, C. L., Sparks, R. S. J. & Carroll, M. R. Experimental constraints on the conditions of formation of highly calcic plagioclase microlites at the Soufrire Hills Volcano, Montserrat. *J. Petrol.* **44**,1455-1475 (2003).

26. Shea, T. & Hammer, J. E. Kinetics of cooling-and decompression-induced crystallization in hydrous mafic-intermediate magmas. *J. Volcanol. Geotherm. Res.* **260**, 127-145 (2013).

27. Agostini, C., Fortunati, A., Arzilli, F., Landi, P. & Carroll, M. R. Kinetics of crystal evolution as a probe to magmatism at Stromboli (Aeolian Archipelago, Italy). *Geochim. Cosmochim. Acta* **110**, 135-151 (2013).

28. Vona, A. & Romano, C. The effects of undercooling and deformation rates on the crystallization kinetics of Stromboli and Etna basalts. *Contrib. Mineral. Petrol.* **166**, 491-509 (2013).

29. Kolzenburg, S., Giordano, D., Hess, K. U. & Dingwell, D. B. Shear Rate Dependent Disequilibrium Rheology and Dynamics of Basalt Solidification. *Geophys. Res. Lett.* **45**, 6466-6475 (2018).

30. Marsh, B. D. On the interpretation of crystal size distributions in magmatic systems. *J. Petrol.* **39**, 553-599 (1998).

31. Cashman, K. V. Relationship between plagioclase crystallization and cooling rate in basaltic melts. *Contrib. Mineral. Petrol.* **113**, 126-142 (1993).

32. Conte, A. M., Perinelli, C. & Trigila, R. Cooling kinetics experiments on different Stromboli lavas: Effects on crystal morphologies and phases composition. *J. Volcanol. Geotherm. Res.* **155**, 179-200 (2006).

33. Szramek, L., Gardner, J. E. & Hort, M. Cooling-induced crystallization of microlite crystals in two basaltic pumice clasts. *Am. Mineral.* **95**, 503-509 (2010).

34. Brugger, C. R. & Hammer, J. E. Crystallization kinetics in continuous decompression experiments: implications for interpreting natural magma ascent processes. *J. Petrol.* **51**, 1941-1965 (2010).

35. Karagadde, S., Lee, P. D., Cai, B., Fife, J. L., Azeem, M. A., Kareh, K. M., Puncreobutr, C., Tsivoulas, D., Connolley, T. & Atwood, R. C. Transgranular liquation cracking of grains in the semi-solid state. *Nature Commun.* **6**, 8300 (2015).

36. Polacci, M., Arzilli, F., La Spina, G., Le Gall, N., Cai, B., Hartley, M. E., Di Genova, D., Vo, N. T., Nonni, S., Atwood, R. C., Llewellin, E. W., Lee, P. D. & Burton, M. R. Crystallisation in basaltic magmas revealed via in situ 4D synchrotron X-ray microtomography. *Sci. Rep.* **8**, 8377 (2018).

37. Goepfert, K. & Gardner, J. E. Influence of pre-eruptive storage conditions and volatile contents on explosive Plinian style eruptions of basic magma. *Bull. Volcanol.* **72**, 511-521 (2010).

38. Szramek, L. A. Mafic Plinian eruptions: Is fast ascent required? *J. Geophys. Res.: Solid Earth* **121**, 7119-7136 (2016).

39. Suzuki, Y. & Fujii, T. Effect of syneruptive decompression path on shifting intensity in basaltic sub-Plinian eruption: Implication of microlites in Yufune-2 scoria from Fuji volcano, Japan. *J. Volcanol. Geotherm. Res.* **198**, 158-176 (2010).

40. Campagnola, S., Romano, C., Mastin, L. G. & Vona, A. Confort 15 model of conduit dynamics: applications to Pantelleria Green Tuff and Etna 122 BC eruptions. *Contrib. Mineral. Petrol.* **171**, 60 (2016).

41. Cassidy, M., Manga, M., Cashman, K. & Bachmann, O. Controls on explosive-effusive volcanic eruption styles. *Nature Commun.* **9**, 2839 (2018).

42. Zhang, Y., Ni, H. & Chen, Y. Diffusion data in silicate melts. *Rev. Mineral. Geochem.* **72**, 311-408 (2010).

43. Namiki, A. & Manga, M. Transition between fragmentation and permeable outgassing of low viscosity magmas. *J. Volcanol. Geotherm. Res.* **169**, 48-60 (2008).

**Methods references section**

44. Corsaro, R. A., Miraglia, L. & Pompilio, M. Petrologic evidence of a complex plumbing system feeding the July-August 2001 eruption of Mt. Etna, Sicily, Italy. *Bull. Volcanol.* **69**, 401–421 (2007).

45. Lesne, P., Scaillet, B., Pichavant, M., Iacono-Marziano, G. & Beny, J. M. The H 2 O solubility of alkali basaltic melts: an experimental study. *Contrib. Mineral. Petrol.* **162**, 133-151 (2011).

46. Drakopoulos, M., Connolley, T., Reinhard, C., Atwood, R., Magdysyuk, O., Vo, N., Hart, M., Connor, L., Humphreys, B., Howell, G. & Davies, S. I12: the joint engineering, environment and processing (JEEP) beamline at diamond light source. *J. Synchrotron Radiat.* **22**, 828-838 (2015).

47. Azeem, M. A., Lee, P. D., Phillion, A. B., Karagadde, S., Rockett, P., Atwood, R. C., Courtois, L., Rahman, K. M. & Dye, D. Revealing dendritic pattern formation in Ni, Fe and Co alloys using synchrotron tomography. *Acta Materialia* **128**, 241-248 (2017).

48. Cloetens, P., Barrett, R., Baruchel, J., Guigay, J. P. & Schlenker, M. Phase objects in synchrotron radiation hard X-ray imaging. *J. Phys. D. Appl. Phys.* **29**, 133–46 (1996).

49. O'sullivan, J. D. A fast sinc function gridding algorithm for Fourier inversion in computer tomography. *IEEE T. Med. Imaging* **4**, 200-207 (1985).

50. Gürsoy, D., De Carlo, F., Xiao, X. & Jacobsen, C. TomoPy: a framework for the analysis of synchrotron tomographic data. *J. Synchrotron Radiat.* **21**, 1188-1193 (2014).

51. Vo, N. T., Drakopoulos, M., Atwood, R. C. & Reinhard, C. Reliable method for calculating the center of rotation in parallel-beam tomography. *Opt. Express* **22**, 19078–19086 (2014).

52. Vo, N. T., Atwood, R. C. and Drakopoulos, M. Superior techniques for eliminating ring artifacts in X-ray micro-tomography. *Opt. Express* **26**, 28396-28412 (2018).

53. Titarenko, S., Withers, P. J. & Yagola, A. An analytical formula for ring artefact suppression in X-ray tomography. *Appl. Math. Lett.* **23**, 1489-1495 (2010).

54. Abramoff M. D., Magalhaes P. J. & Ram S. J. Image processing with ImageJ. *Biophot. Int.* **11**, 36–42 (2004).

55. Arzilli, F., Mancini, L., Voltolini, M., Cicconi, M. R., Mohammadi, S., Giuli, G., Mainprice, D., Paris, E., Barou, F. & Carroll, M. R. Near-liquidus growth of feldspar spherulites in trachytic melts: 3D morphologies and implications in crystallization mechanisms. *Lithos* **216**, 93-105 (2015).

56. Arzilli, F., Polacci, M., Landi, P., Giordano, D., Baker, D. R. & Mancini, L. A novel protocol for resolving feldspar crystals in synchrotron X-ray microtomographic images of crystallized natural magmas and synthetic analogs. *Am. Mineral.* **101**, 2301-2311 (2016).

57. Brun, F., Mancini, L., Kasae, P., Favretto, S., Dreossi, D. & Tromba, G. Pore3D: a software library for quantitative analysis of porous media. *Nucl. Instrum. Meth. A* **615**, 326–332 (2010).

58. Ohser, J. & Mücklich, F. Statistical analysis of microstructure in material science. Barnett V, editor. Statistics in Practice, West Sussex, England: John Wiley & Sons; (2000).

59. La Spina, G., Polacci, M., Burton, M. & de' Michieli Vitturi, M. Numerical investigation of permeability models for low viscosity magmas: application to the 2007 Stromboli effusive eruption *Earth Planet. Sci. Lett.* **473**, 279-290 (2017).

60. de' Michieli Vitturi, M., Clarke, A. B., Neri, A. & Voight, B. Transient effects of magma ascent dynamics along a geometrically variable dome-feeding conduit. *Earth Planet. Sci. Lett.* **295**, 541–553 (2010).

61. Caricchi, L., Burlini, L., Ulmer, P., Gerya, T., Vassalli, M. & Papale, P. Non-Newtonian rheology of crystal-bearing magmas and implications for magma ascent dynamics. *Earth Planet. Sci. Lett.* **264**, 402–419 (2007).

62. Giordano, D., Russell, J. K. & Dingwell, D. B. Viscosity of magmatic liquids: a model. *Earth Planet. Sci. Lett.* **271**, 123-134 (2008).

63. Del Carlo, P. & Pompilio, M. The relationship between volatile content and the eruptive style of basaltic magma: the Etna case. *Ann. Geophys.* **47** (2004).

64. Costa, A., Caricchi, L. & Bagdassarov, N. A model for the rheology of particle-bearing suspensions and partially molten rocks. *Geochem. Geophys. Geosyst.* **10**, (2009).

65. Vona, A., Romano, C., Dingwell, D. & Giordano, D. The rheology of crystal-bearing basaltic magmas from Stromboli and Etna. *Geochim. Cosmochim. Acta* **75**, 3214–3236 (2011).

66. Smith, P. M. & Asimow, P. D. Adiabat_1ph: a new public front-end to the MELTS, pMELTS, and pHMELTS models. *Geochem. Geophys. Geosyst.* **6**, (2005).

67. Ghiorso, M. S. & Sack, R. O. Chemical mass transfer in magmatic processes IV. A revised and internally consistent thermodynamic model for the interpolation and extrapolation of liquid–solid equilibria in magmatic systems at elevated temperatures and pressures. *Contrib. Mineral. Petrol.* **119**, 197–212 (1995).

68. Adams, B. M., Ebeida, M. S., Eldred, M. S., Geraci, G., Jakeman, J. D., Maupin, K. A., Monschke, J. A., Swiler, L. P., Stephens, J. A., Vigil, D. M., Wildey, T. M., Bohnhoff, W. J., Dalbey, K. R., Eddy, J. P., Frye, J. R., Hooper, R. W., Hu, K. T., Hough, P. D., Khalil, M., Ridgway, E. M. & Rushdi, A. DAKOTA, A Multilevel Parallel Object-Oriented Framework for Design Optimization, Parameter Estimation, Uncertainty Quantification, and Sensitivity Analysis Version 6.6 User's Manual Tech. rep., SAND2014-4633, Tech. rep., SAND2014-4633, (2017).

**Correspondence and requests for materials** should be addressed to F.A. (fabio.arzilli@manchester.ac.uk)

**Acknowledgements**

The research leading to these results has received funding from the RCUK NERC DisEqm project (NE/N018575/1) and (NE/M013561/1). The beamtime on I12 was provided by Diamond Light Source (EE16188-1) and laboratory space by the Research Complex at Harwell. Sensitivity analyses were performed on the ARCHER National Supercomputing Service (UK).

**Author Contributions**

M.P., F.A., M.R.B., and P.D.L. conceived the research project. F.A., M.P., G.L.S., N.L.G., B.C., M.E.H., D.D.G., N.T.V., S.N., R.C.A., E.W.L., P.D.L., H.M.M. and M.R.B. contributed to the beamline experiments. F.A. collected the volcanic rocks for the starting material. D.D.G., H.M.M and R.A.B. prepared the starting material. F.A., M.P., G.L.S. and N.T.V. performed image reconstruction. F.A. and M.P. performed image processing. F.A. performed image segmentation and analysis. G.L.S. performed numerical simulations using the conduit model. R.A.B. and F.A. performed *ex situ* decompression experiments. F.A. and M.E.H performed chemical analysis. E.C.B., F.A. and G.L.S. collected samples of the Etna 122 B.C. Plinian eruption. E.C.B. and F.A. acquired and analysed back-scattered electron images of Etna 122 B.C. Plinian eruption samples. F.A., G.L.S., M.R.B., M.P. and E.C.B. wrote the manuscript, with contributions from all other authors.

**Competing interests**

The authors declare no competing financial interests.

**Additional information**

**Supplementary information** is available in the online version of the paper.

**Reprints and permissions information** is available at www.nature.com/reprints.

## FIGURES

**Figure 1. Crystallisation through time during experiment ET1150**. Reconstructed axial slices during continuous cooling at 0.4 °$Cs^{-1}$: **a**, frame represents the texture after 114 s from the onset of the cooling in which the temperature ranges between 1144 and 1112 °C (average 1128 °C); **b,** frame after 294 s, in which the temperature ranges between 1073 and 1034 °C (average 1054 °C); **c,** frame after 474 s, in which the temperature ranges between 997 and 959 °C (average 978 °C). m = melt; Plg = plagioclase; Cpx = clinopyroxene; Ti-Mag: titanomagnetite. The acquisition time of each frame is 90 s. t = time from the onset of the cooling to the end of the frame acquisition.

**Figure 2. Plagioclase crystal morphology**. **a**, The 3D volume rendering of sample ET1150 shows the morphology and the spatial distribution of plagioclase crystals that formed during the rapid cooling at $96<\Delta T<155$ °C. **b**, 3D view of the plagioclase with swallow-tailed crystal morphology. **c**, Back scattered electron image of plagioclase with swallow-tailed crystal morphology. **d**, Back scattered electron image of plagioclase with swallow-tailed crystal morphology produced during the Etna 122 B.C Plinian eruption. Note heterogeneous nucleation of pyroxene around plagioclase, seen as a light-coloured halo, and similar to that seen in Fig. 1b.

**Figure 3. Model results during magma ascent**. **a**, Undercooling as a function of depth, calculated for $\tau(c)$ = 10 (blue) and 1000 s (red). Cooling is driven by adiabatic expansion of gas, mitigated by latent heat of crystallisation particularly in the fast crystallising case. **b**, Crystal content in vol%, demonstrating the rapid increase in crystal load when $\tau(c)$ = 10 s. **c**, Magma viscosity, demonstrating that the higher crystal load produces 3-4 order of magnitude increase in viscosity, leading to fragmentation.

**Figure 4. Sensitivity analyses.** Relationships between characteristic time, initial temperature, initial $H_2O$ content of the magma, syn-eruptive crystal content and magma viscosity and the undercooling of the system at the fragmentation level. These figures were calculated using repeated runs of the model while changing individual parameters to reveal the sensitivity of the system to each parameter. Likelihood of explosive eruption as a function of a specific parameter arises from the ratio between the number of model runs producing explosive eruptions divided by the total number of model runs used to test that parameter. Therefore, this is not a probabilistic assessment of eruption risk, but instead depends on the critical model parameters, which control when fragmentation occurs, and the calculated probabilities depend on the choice of upper and lower limits chosen for each investigated parameter. **a**, Sobol index. **b**, Undercooling vs magma temperature before ascent. The error bars represent the spread of these output values with respect to the corresponding mean. **c**, Undercooling vs the initial $H_2O$ content of the magma (dissolved and exsolved). For a given input value, the solid lines are the mean of a given output parameter obtained from all the simulations assuming that input value. The error bars represent the spread of the output values with respect to the corresponding mean. **d**, Frequency of explosive eruptions vs magma temperature before ascent. **e**, Explosion frequency vs initial phenocryst content. **f**, Frequency of explosive eruptions vs syn-eruptive crystal content at the fragmentation level. **g**, Frequency of explosive eruptions vs magma viscosity at the fragmentation level.

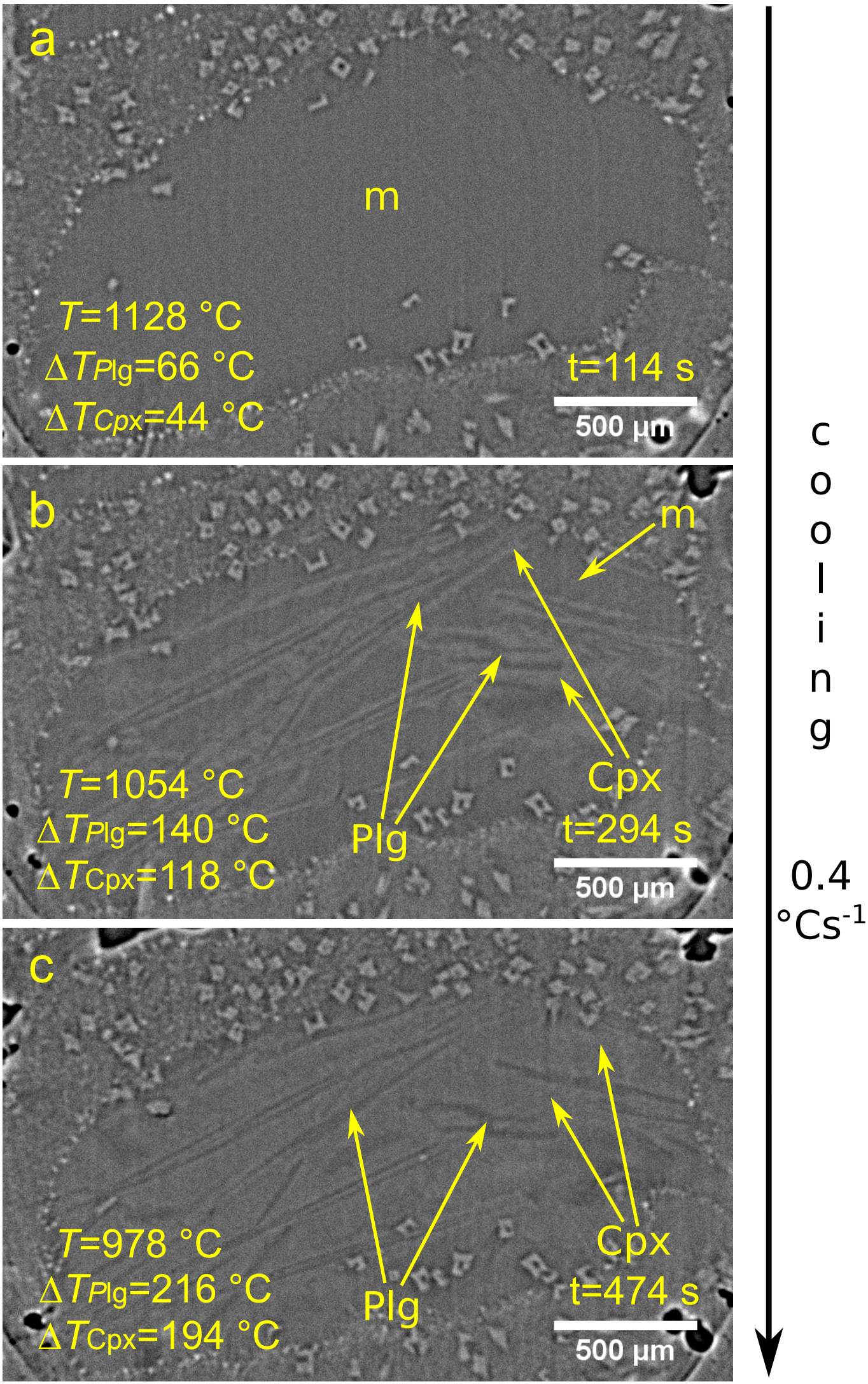
a
m
T=1128 °C
ΔTPlg=66 °C
ΔTCpx=44 °C
t=114 s
500 µm
b
m
Plg
Cpx
T=1054 °C
ΔTPlg=140 °C
ΔTCpx=118 °C
t=294 s
500 µm
c
Plg
Cpx
T=978 °C
ΔTPlg=216 °C
ΔTCpx=194 °C
t=474 s
500 µm
cooling
0.4
°Cs-1

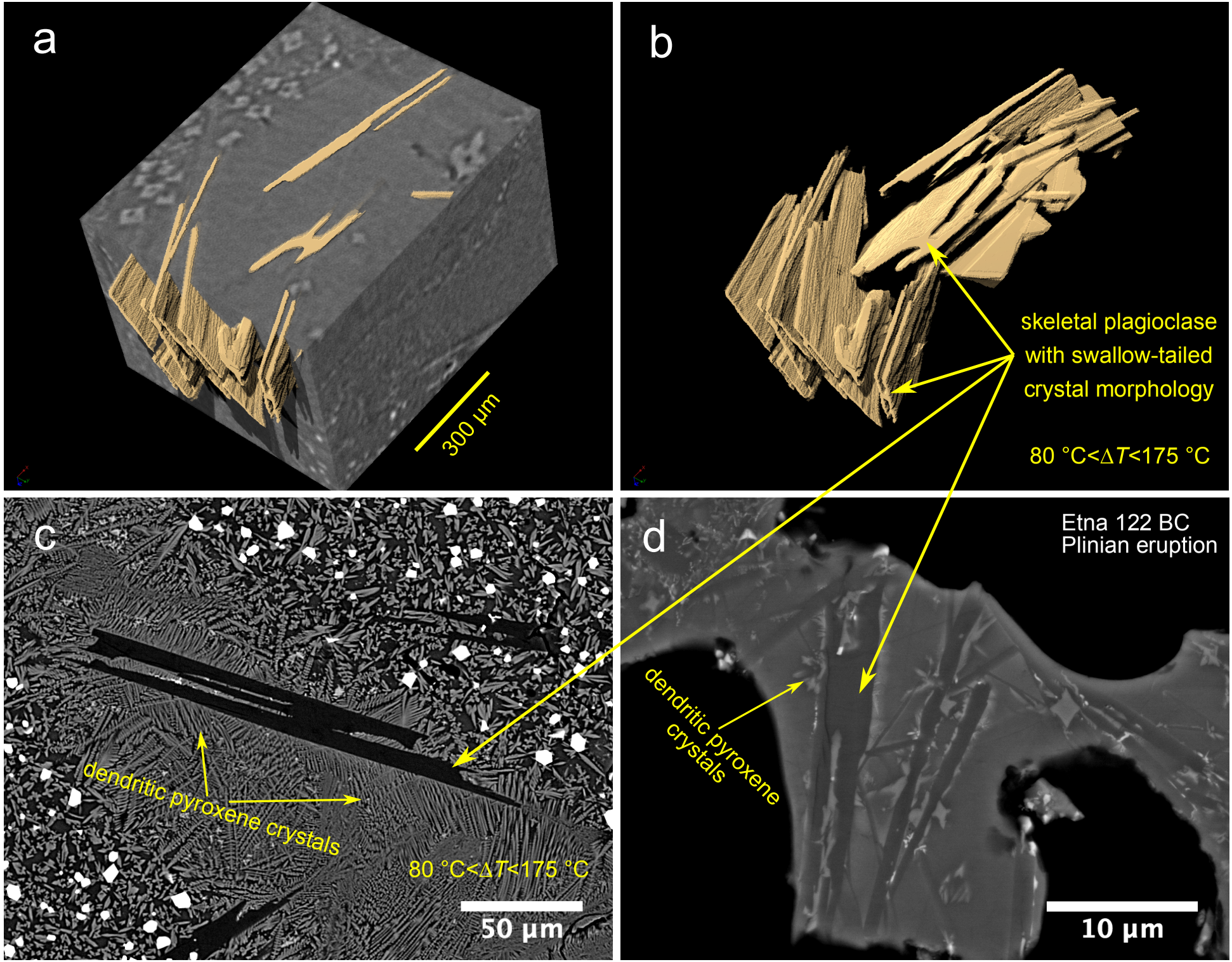
a
300 µm
b
skeletal plagioclase
with swallow-tailed
crystal morphology
80 °C<ΔT<175 °C
c
dendritic pyroxene crystals
80 °C<ΔT<175 °C
50 µm
d
Etna 122 BC
Plinian eruption
dendritic pyroxene
crystals
10 µm

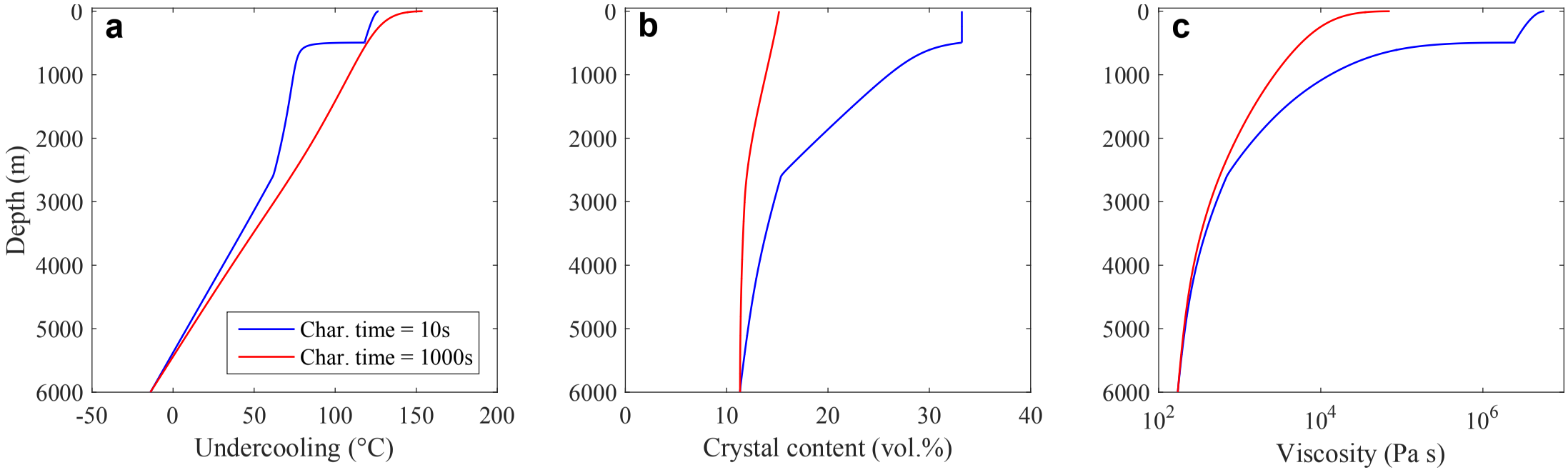
a
b
c
Depth (m)
0
1000
2000
3000
4000
5000
6000
-50
0
50
100
150
200
Undercooling (°C)
Char. time = 10s
Char. time = 1000s
10
20
30
40
Crystal content (vol.%)
$10^2$
$10^4$
$10^6$
Viscosity (Pa s)

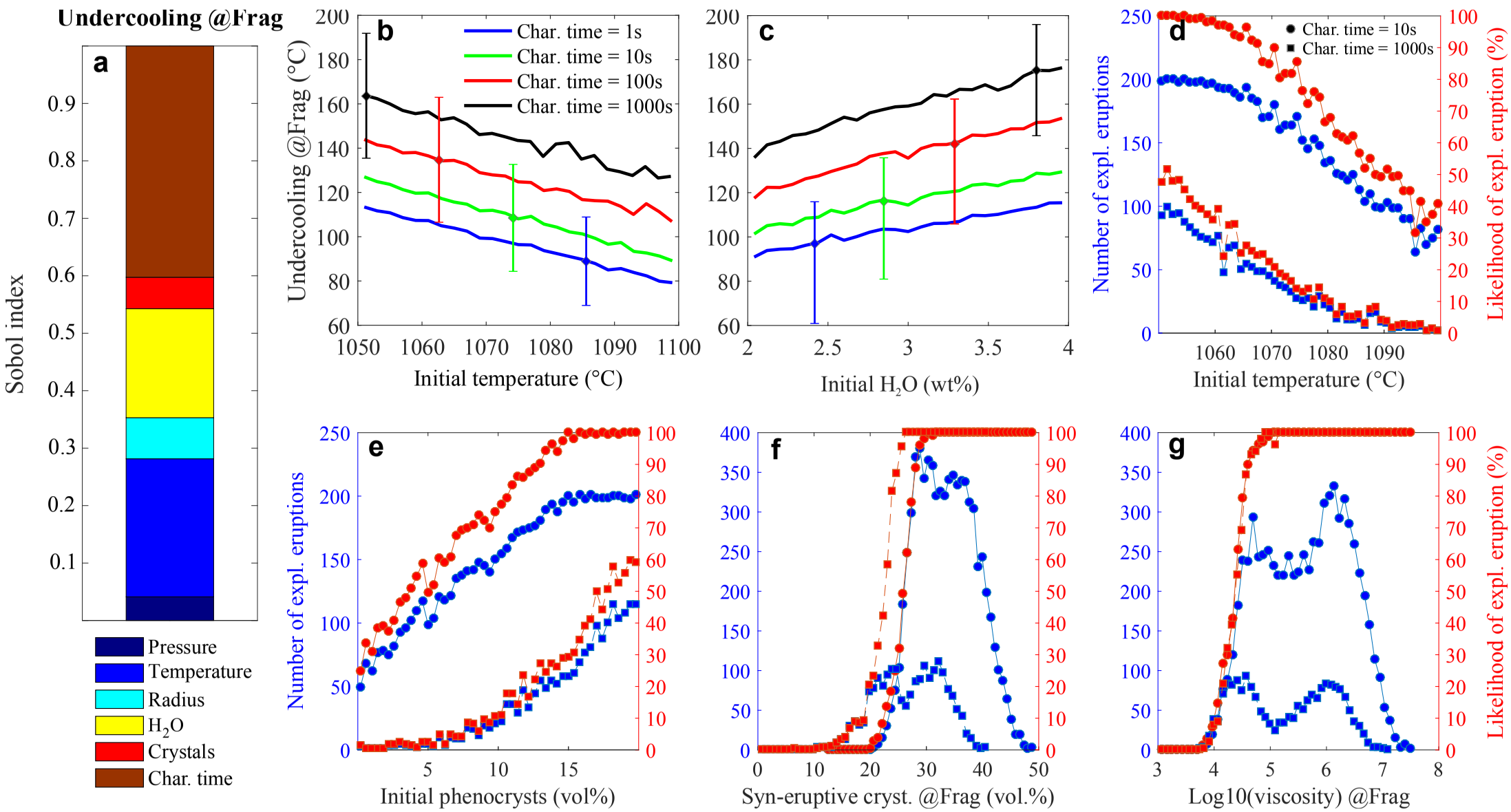
Undercooling @Frag
a
Sobol index
Pressure
Temperature
Radius
H2O
Crystals
Char. time
b
Undercooling @Frag (°C)
Char. time = 1s
Char. time = 10s
Char. time = 100s
Char. time = 1000s
Initial temperature (°C)
c
Initial H2O (wt%)
d
Number of expl. eruptions
Likelihood of expl. eruption (%)
Char. time = 10s
Char. time = 1000s
Initial temperature (°C)
e
Number of expl. eruptions
Initial phenocrysts (vol%)
f
Syn-eruptive cryst. @Frag (vol.%)
g
Likelihood of expl. eruption (%)
Log10(viscosity) @Frag